

21 cm Angular Power Spectrum from Minihalos as a Probe of Primordial Spectral Runnings

Toyokazu Sekiguchi,^a Tomo Takahashi,^b Hiroyuki Tashiro^c and Shuichiro Yokoyama^d

^aCenter for Theoretical Physics of the Universe, Institute for Basic Science, Daejeon 34051, Korea

^bDepartment of Physics, Saga University, Saga 840-8502, Japan

^cDepartment of Physics, Graduate School of Science, Nagoya University, Aichi 464-8602, Japan

^dDepartment of Physics, Rikkyo University, 3-34-1 Nishi-Ikebukuro, Toshima, Tokyo 171-8501, Japan

E-mail: sekiguti@ibs.re.kr, tomot@cc.saga-u.ac.jp, hiroyuki.tashiro@nagoya-u.jp, shuichiro@rikkyo.ac.jp

Abstract. Measurements of 21 cm line fluctuations from minihalos have been discussed as a powerful probe of a wide range of cosmological models. However, previous studies have taken into account only the pixel variance, where contributions from different scales are integrated. In order to sort out information from different scales, we formulate the angular power spectrum of 21 cm line fluctuations from minihalos at different redshifts, which can enhance the constraining power enormously. By adopting this formalism, we investigate expected constraints on parameters characterizing the primordial power spectrum, particularly focusing on the spectral index n_s and its runnings α_s and β_s . We show that future observations of 21 cm line fluctuations from minihalos, in combination with cosmic microwave background, can potentially probe these runnings as $\alpha_s \sim \mathcal{O}(10^{-3})$ and $\beta_s \sim \mathcal{O}(10^{-4})$. Its implications to the test of inflationary models are also discussed.

Contents

1	Introduction	1
2	Angular power spectrum of 21 cm line fluctuations from minihalos	3
3	Fisher matrix analysis	6
4	Constraints on spectral runnings of primordial power spectrum	8
4.1	Runnings of the spectral index	8
4.2	Forecasts based on the Fisher matrix analysis	8
4.3	Implication for the constraint on the inflationary models	12
4.3.1	R^2 -inflation	13
4.3.2	Brane inflation	14
4.3.3	Natural-spectator model	15
4.3.4	Inverse monomial-spectator model	16
4.3.5	Predictions of the models	16
5	Conclusion	18
A	Expressions for higher order runnings with slow-roll parameters	18
A.1	Single-field case	19
A.2	Multi-field case	19
B	Constraints on higher order spectral runnings	21

1 Introduction

Current precise measurements of the cosmic microwave background (CMB) from Planck [1, 2] and other cosmological observations, such as baryon acoustic oscillation (BAO) (see e.g., [3]), type Ia supernovae (SNe) (see e.g., [4]) and so on, have unveiled various aspects of the Universe from the very early time to the present. The very early Universe can be probed by investigating primordial fluctuations whose properties can be measured by observing the CMB anisotropies and large scale structures of the Universe. Since the primordial fluctuations are considered to be generated during inflation, by studying the properties of the primordial fluctuations, we can test inflationary models and generation mechanisms of these fluctuations.

The measurement of the CMB by Planck in combination with other observations has provided strong constraints on inflationary parameters describing the nature of primordial fluctuations such as their amplitude A_s , the spectral index n_s , the tensor-to-scalar ratio r and the non-linearity parameter f_{NL} [5]. However, we are still far from specifying the model of inflation and more observational information is required to fully understand the very early epoch of the Universe.

Among the inflationary parameters, the tensor-to-scalar ratio is one of the promising quantity which, in the near future, can be probed more accurately from on-going and planned CMB B-mode polarization experiments (see, e.g., [6–10]). Since the tensor-to-scalar ratio is directly related to the energy scale of inflation, its information would give important

implications to the models of inflation. Another property of primordial fluctuations worth investigating is their scale-dependence, which is usually represented by the spectral index n_s . Although n_s at a reference wavenumber on large scales is accurately determined by Planck data [5], it also depends on the scale in general. The scale-dependence of n_s is commonly denoted as the running α_s , which is defined as $\alpha_s = dn_s/d\ln k$. Furthermore, α_s also generally depends on the scale, which is referred as the running of the running $\beta_s = d^2n_s/d\ln^2 k$. Compared to n_s , the current constraints on these runnings are not so severe even with the Planck data [5]. However, these can be probed more precisely by future observations on smaller scales such as 21 cm line fluctuations from the intergalactic medium (IGM) [11, 12], the CMB spectral μ distortion [13, 14] and galaxy surveys [12].

We in this paper argue that future observations for the angular power spectrum of 21 cm line fluctuations from minihalos, which are virialized objects with the virial temperature $T < 10^4$ K, would be a useful probe of the shape of the primordial power spectrum. Since the virial temperature of minihalos is not high enough to cause the effective collisional ionization, the inside of a minihalo is filled with dense neutral gas. Therefore, the existence of minihalos can induce the additional 21 cm line signals [15, 16]. Since the abundance of minihalos depends on the matter density fluctuations at $20 \text{ Mpc}^{-1} < k < 500 \text{ Mpc}^{-1}$, the 21 cm signatures from minihalos have been discussed as a probe of various cosmological models, particularly on small scales. In Ref. [17], the potential to probe small-scale primordial fluctuations has been investigated by using absorption features produced by minihalos in the continuum spectrum of the radio sources at high redshifts.

The clustering of minihalos has also been studied in the context of warm dark matter [18], isocurvature fluctuations [19, 20], primordial non-Gaussianity [21], cosmic strings [22] and so on, because the clustering can enhance the fluctuations of 21 cm line signals related to the matter density fluctuations. In other words, minihalos are biased tracers of the matter density fluctuations. Once we measure how much the 21 cm line fluctuations are biased by minihalos, we can probe matter fluctuations on much smaller scales compared with CMB or large scale structure observations. However, in these previous studies, only the pixel variance of 21 cm line fluctuations has been focused on to investigate the feasibility of future 21 cm line observations. Although the pixel variance would be easy to obtain from actual observational data, it cannot tell us the contributions from different scales. Hence, instead of the pixel variance, we discuss the 21 cm line signals from minihalos in terms of the angular power spectrum which can probe the contributions from different scales. We show that the next generation 21 cm survey such as Square Kilometre Array (SKA) [23] and Fast Fourier Transform Telescope (FFTT) [24] can measure the scale-dependence very accurately, which will be very helpful to differentiate models of inflation.

The structure of this paper is as follows. In the next section, we describe the formalism to calculate the angular power spectrum of 21 cm line fluctuations from minihalos. Then in Section 3, we discuss the Fisher matrix for the angular power spectrum of 21 cm line fluctuations as well as that for CMB. In Section 4, we estimate expected constraints on the power spectrum of primordial perturbations, focusing on the runnings of the spectral index, assuming future 21 cm surveys including SKA and FFTT in combination with CMB observations. Implications for specific models for inflation are also discussed here. We conclude in the final section. In Appendix A, we present general expressions for the spectral parameters for single-field inflation models and multi-field ones with the inflaton and spectator fields. In Appendix B, constraints on higher order spectral runnings are given.

2 Angular power spectrum of 21 cm line fluctuations from minihalos

Minihalos are neutral virial objects which are enough dense to decouple the spin temperature of neutral hydrogen from the CMB temperature and can produce the observable 21 cm signal. Since minihalos are biased objects of the matter density fluctuations, the abundance of minihalos also fluctuates. As a result, the fluctuations of 21 cm signals due to minihalos arise. Here, following the treatment of the previous works [15, 16, 18–22], we derive the angular power spectrum of 21 cm line fluctuations from minihalos.

We are interested in 21 cm line fluctuations on scales which are much larger than the typical formation scale of minihalos. In other words, the angular resolution of an observation is much larger than the size of individual minihalos. In this case, there exist multiple minihalos in a beam size of the observation. The observable of 21 cm measurements is written in terms of the differential brightness temperature, which represents the deviation of the brightness temperature from the CMB temperature. The mean differential brightness temperature due to minihalos at redshift z can be obtained from [15]

$$\overline{\Delta T_b}(z) = c \frac{(1+z)^4}{H(z)\nu_0} \int_{M_{\min}}^{M_{\max}} dM \frac{dn}{dM} \Delta\nu_{\text{eff}} A \langle \delta T_b \rangle, \quad (2.1)$$

where ν_0 is the frequency corresponding to 21 cm, $\Delta\nu_{\text{eff}} = [\phi(\nu_0)(1+z)]^{-1}$ with the intrinsic line profile $\phi(\nu_0)$ of a minihalo, dn/dM is a mass function of minihalos, A is the cross-section of a minihalo, and $\langle \delta T_b \rangle$ is the typical brightness temperature of a minihalo averaged over the cross-section A . We consider that minihalos are in the mass range between M_{\max} and M_{\min} . We set M_{\max} and M_{\min} to the virial mass with the virial temperature $T_{\text{vir}} = 10^4$ K and the Jeans mass, respectively. As dn/dM , we adopt the Press-Schechter mass function. The nature of minihalos, e.g., the profiles of the gas density and pressure, determines A , $\phi(\nu_0)$ and $\langle \delta T_b \rangle$. Here we use a truncated isothermal sphere as the model of a minihalo, which depends on the minihalo mass M [25]. Minihalos are clustered, depending on the underlying density fluctuations. Therefore, 21 cm line fluctuations from minihalos at a redshift z in the line-of-sight direction \hat{n} should be written as (neglecting the redshift space distortions) [15, 18, 20]

$$\delta\Delta T_b(\hat{n}, z) = \overline{\Delta T_b}(z) \beta(z) \delta(\vec{x} = r(z)\hat{n}, z), \quad (2.2)$$

where $\beta(z)$ is the effective bias of minihalos, $\delta(\vec{x}, z)$ represents the matter density fluctuations at the comoving coordinates \vec{x} and redshift z , and $r(z)$ is the comoving distance from us to the redshift z . The effective bias $\beta(z)$ is given as

$$\beta(z) \equiv \frac{\int_{M_{\min}}^{M_{\max}} dM \frac{dn}{dM} \mathcal{F}(z, M) b(M, z)}{\int_{M_{\min}}^{M_{\max}} dM \frac{dn}{dM} \mathcal{F}(z, M)}, \quad (2.3)$$

where $\mathcal{F} = \langle \delta T_b \rangle A \sigma_V$ with the velocity dispersion of a minihalo σ_V and $b(M, z)$ being the bias of minihalos with mass M for which we adopt one obtained in Ref. [26]. We refer the readers to Refs. [15, 18, 20] for the detailed derivation of $\overline{\Delta T_b}(z)$ and $\beta(z)$.

Minihalos discussed in this paper are collapsed objects and the corresponding scales of matter density fluctuations are at $20 \text{ Mpc}^{-1} < k < 500 \text{ Mpc}^{-1}$ [18]. Therefore, the bias (clustering) as well as the mean number density of minihalos depends on the fluctuations at these scales. As shown in Eq. (2.2) with Eq. (2.3), the clustering enhances the signals of 21 cm fluctuations over all scales. As a result, the measurement of the 21 cm line fluctuation

amplitude provides useful information about the matter density fluctuations on small scales where minihalos form.

Although we focus on the 21 cm signals from minihalos in this paper, the IGM also contributes to the signal, which can be written as

$$\Delta T_{b\text{IGM}} \approx 28\text{mK} \sqrt{\frac{z+1}{10}} x_{\text{HI}}(z)(1+\delta)(1-T_{\text{CMB}}/T_s), \quad (2.4)$$

where $x_{\text{HI}}(z)$ and T_s are the neutral fraction and the spin temperature of the IGM, respectively [27]. Which contribution dominates the signal, from minihalos or the IGM, depends on the thermal and ionization history of the IGM. In general, the reionization process proceeds faster in the IGM than in minihalos [28]. This is because minihalos are $\mathcal{O}(100)$ times denser than the IGM. Accordingly much more ionizing background photons are required to ionize minihalos in comparison with the IGM. In this paper, for simplicity, we assume that minihalos are not ionized at all until the completion of reionization. Under this assumption, Fig. 1 compares the signal of the 21 cm line fluctuations from minihalos, $\overline{\Delta T_b}(z)\beta$, with that of the IGM $\overline{\Delta T_{b\text{IGM}}}$ given in Eq. (2.4). In the figure, we assume a rapid reionization with the optical depth $\tau_{\text{reion}} = 0.058$ and the width of the duration $\Delta z = 1$ in accordance with the recent Planck result [29] for $x_{\text{HI}}(z)$ to calculate the signal from the IGM. We obtain the spin temperature, taking the simple model of the IGM gas temperature evolution in which the gas temperature is proportional to x_{HI} during the reionization and reaches 10^4 K when the reionization completes [30]. The figure shows that the signal from minihalos can surpass that from IGM in almost overall redshifts. Although, as mentioned above, the signal from the IGM depends on the reionization history, we have also checked other several models and found that, even if we change the reionization history, the signal from minihalos dominates for some redshift range. Therefore, in the following analysis, we neglect the contribution from the IGM. We also note that the contribution from minihalos is dominant in the end of the dark ages ($15 < z < 40$). At this epoch, the temperature of the IGM is so low that the spin temperature is almost same as the CMB temperature. Therefore, the signals from the IGM are suppressed. However, as we will discuss later, the observational noise becomes large as the observation redshift increases. Hence we consider the signals only from $z < 20$ in our analysis.

Given a redshift z , we consider maps of the 21 cm line fluctuations $\delta\Delta T_b(\hat{n}, z)$ and matter ones $\delta(r(z)\hat{n}, z)$ in the sky. They can be transformed into the spherical harmonic coefficients as

$$a_{lm}^{(21\text{cm})}(z) = \int d\hat{n} \delta\Delta T_b(\hat{n}, z) Y_{lm}^*(\hat{n}), \quad (2.5)$$

$$a_{lm}^{(\text{matter})}(z) = \int d\hat{n} \delta(r(z)\hat{n}, z) Y_{lm}^*(\hat{n}). \quad (2.6)$$

Due to the statistical isotropy of the matter fluctuations, the angular power spectrum of the 21 cm line fluctuations from minihalos should be given as

$$C_l^{(21\text{cm})}(z, z') = \overline{\Delta T_b}(z)\overline{\Delta T_b}(z')\beta(z)\beta(z')C_l^{(\text{matter})}(z, z'), \quad (2.7)$$

where $C_l^{(21\text{cm})}(z, z')$ and $C_l^{(\text{matter})}(z, z')$ are respectively the angular power spectra of 21cm line fluctuations and the matter ones between redshifts z and z' , whose definitions are

$$\langle a_{lm}^{(21\text{cm})}(z) a_{l'm'}^{(21\text{cm})*}(z') \rangle = C_l^{(21\text{cm})}(z, z') \delta_{ll'} \delta_{mm'}, \quad (2.8)$$

$$\langle a_{lm}^{(\text{matter})}(z) a_{l'm'}^{(\text{matter})*}(z') \rangle = C_l^{(\text{matter})}(z, z') \delta_{ll'} \delta_{mm'}. \quad (2.9)$$

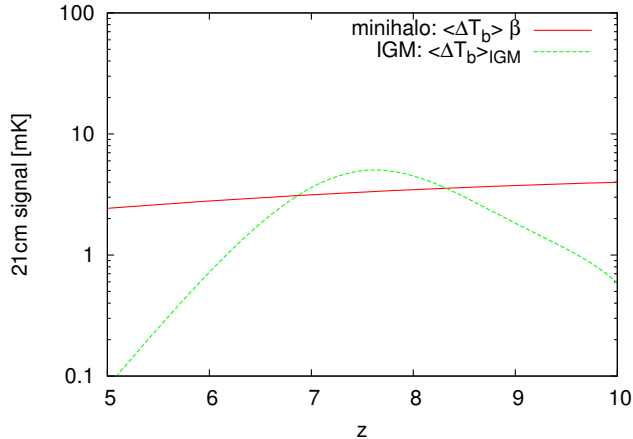


Figure 1. Comparison of the signals in 21 cm line fluctuations from minihalos (red solid line) and the IGM (green dashed line) as functions of redshift z . For the IGM signal, we have assumed a rapid reionization with the optical depth $\tau_{\text{reion}} = 0.058$ and the width of the duration $\Delta z = 1$ in accordance with the recent result [29].

The angular power spectrum of matter fluctuations $C_l^{(\text{matter})}$ can be related to the matter power spectrum $P(k)$ as

$$C_l^{(\text{matter})}(z, z') = D(z)D(z') \int \frac{k^2 dk}{2\pi^2} P(k) j_l(kr(z)) j_l(kr(z')), \quad (2.10)$$

where $D(z)$ is the growth factor relative to a reference redshift z_{ref} (i.e., $\delta(k, z) = D(z)\delta(k, z_{\text{ref}})$ with $\delta(k, z)$ being the matter fluctuations in the k -space) and the linear matter power spectrum at a reference redshift z_{ref} is denoted as $P(k)$. j_l is the spherical Bessel function. In the redshift range we consider in the following analysis, the Universe is well approximated as matter-dominated, in which $D(z)$ is given by $D(z) \propto a(z)$, with $a(z)$ being the scale factor at z .

So far we have neglected the redshift space distortions due to the peculiar velocity of minihalos. Although this effect has not been taken into account in previous studies [15, 16, 18–22], it can be dominant especially in correlations between different redshifts. The redshift space distortions are classified largely into two types. One is the linear effect known as the Kaiser effect while the other is the nonlinear effect called as the Fingers-of-God (FoG) effect [31]. Since we are focusing on the Universe at high redshifts, we expect that the redshift space distortions are weak and can be well-approximated within the framework of the linear perturbation theory. Thus we neglect the FoG effect. Including the Kaiser effect [31], we can rewrite Eq. (2.2) as

$$\delta\Delta T_b(\hat{n}, z) = \overline{\Delta T_b}(z) [\beta(z) + f(z)\mu^2] \delta(\vec{x} = r(z)\hat{n}, z), \quad (2.11)$$

where $\mu = \hat{k} \cdot \hat{n}$ is the cosine between the wave vector of perturbations \vec{k} and line-of-sight direction \hat{n} , and $f = d \ln D / d \ln a$ is the growth rate. Note that in the matter domination

epoch, $f = 1$. After taking account of the redshift space distortions, Eq. (2.10) should then be replaced with

$$C_l^{(\text{matter})}(z, z') = D(z)D(z') \int \frac{k^2 dk}{2\pi^2} P(k) \quad (2.12)$$

$$\times \left[j_l(kr(z)) - \frac{f(z)}{\beta(z)} j_l''(kr(z)) \right] \left[j_l(kr(z')) - \frac{f(z')}{\beta(z')} j_l''(kr(z')) \right],$$

where j_l'' denotes a second derivative with respect to its argument and it should not be confused with a prime attached to z .

In Fig. 2, we plot the angular power spectra $C_l^{(21\text{cm})}(z, z')$ around a central redshift $z = 5$ as an example. The cosmological parameters we assume to calculate $C_l^{(21\text{cm})}(z, z')$ are given in the caption of Fig. 2. From the figure, one can see that the amplitude of the power spectra becomes maximum when the redshift difference, $\Delta z \equiv |z - z'|$, vanishes. Then the amplitude drops as Δz increases, with l being fixed. The correlation at the same redshift, $C_l^{(21\text{cm})}(z, z)$, is almost constant at large angular scales $l \lesssim 100$. In other words, the correlations between different redshifts and different pixels are not very large. This result supports the previous analysis of 21 cm signals from minihalos in which only pixel variance at the same redshift bins are taken into account while the covariance is neglected. However, at smaller angular scales $l \gtrsim 100$, the angular spectrum deviates from the white spectrum $C_l = \text{const.}$, which indicates nonzero covariance between different pixels. In addition, with small but nonzero redshift differences $\Delta z \sim 0.1$, the correlations between different redshifts give non-negligible amplitude. This suggests that, in order to optimally exploit cosmological information in 21 cm line fluctuations from minihalos, we need to take into account the correlation of their fluctuations at different redshifts, too.

3 Fisher matrix analysis

Now we discuss the Fisher matrix for $C_l^{(21\text{cm})}(z, z')$. To calculate the Fisher matrix, we adopt the following observational noise for 21cm line fluctuations. For simplicity, we take the assumption that the noise is white both in angular and frequency domains. Assuming the isotropic Gaussian beam transfer function, we can write the noise power spectrum as [32]

$$N_{l,ij}^{(21\text{cm})} = \delta_{ij} \varsigma_i^2 \Delta\theta_i^2 \exp \left[l(l+1) \frac{\theta_i^2}{8 \ln 2} \right], \quad (3.1)$$

where ς_i is the noise root-mean-squared per pixel and θ_i is the beam width. Following Ref. [33], we approximate ς_i as

$$\varsigma_i = 20\text{mK} \left(\frac{A_{\text{tot}}}{10^4 \text{m}^2} \right)^{-1} \left(\frac{\Delta\theta_i}{10'} \right)^{-2} \left(\frac{1+z_i}{10} \right)^{4.6} \left(\frac{\Delta\nu_i}{\text{MHz}} \frac{t}{100\text{h}} \right)^{1/2}, \quad (3.2)$$

from which one can see that the noise increases as the redshift becomes higher.

Then according to Ref. [34], the Fisher matrix based on a measurement of power spectrum should be given by

$$F_{ab}^{(\text{power})} = \sum_l \frac{2l+1}{2} \text{Tr} \left[\mathbf{C}_l^{(21\text{cm})^{-1}} \frac{\partial \mathbf{C}_l^{(21\text{cm})}}{\partial p_a} \mathbf{C}_l^{(21\text{cm})^{-1}} \frac{\partial \mathbf{C}_l^{(21\text{cm})}}{\partial p_b} \right], \quad (3.3)$$

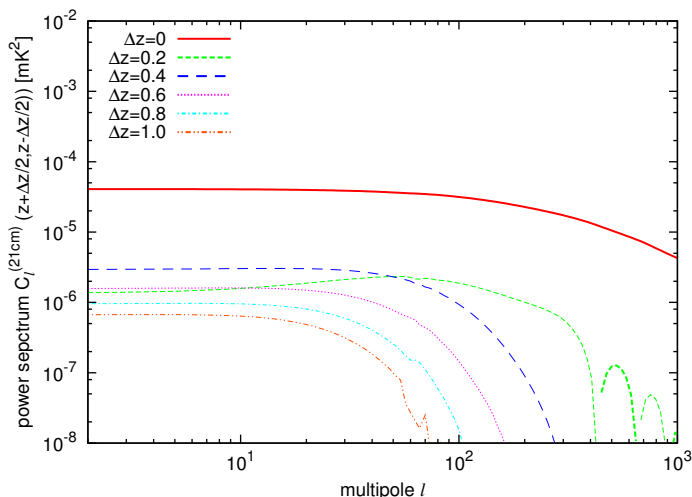


Figure 2. Shown are the angular power spectra of minihalo 21cm line fluctuations $C_l^{(21\text{cm})}(z + \frac{\Delta z}{2}, z - \frac{\Delta z}{2})$ with the central redshift $z = 5$. Thick and thin lines show positive and negative values, respectively. The cosmological parameters are taken to be the mean values of the analysis for a power-law Λ CDM model from Planck 2015 TT,TE,EE+lowP+lensing+ext [2]: CDM density $\omega_c (= \Omega_b h^2) = 0.1188$, baryon density $\omega_b (= \Omega_c h^2) = 0.0223$, the reduced Hubble parameter $h = 0.6774$, the reionization optical depth $\tau_{\text{reion}} = 0.066$, the amplitude and the spectral index of primordial power spectrum (at $k_0 = 0.05 \text{ Mpc}^{-1}$) $A_s = 2.141 \times 10^{-9}$ and $n_s = 0.9667$, respectively.

where p_a (p_b) indicates a cosmological parameter and $[\mathbf{C}_l]_{ij}^{(21\text{cm})} \equiv C_l^{(21\text{cm})} + N_{l,ij}^{(21\text{cm})}$ is the covariant matrix for 21 cm observations.

We again note that we in this paper neglect the contribution from IGM in order to focus on the potential of the measurement of 21cm signals from minihalos. This treatment is also motivated from the fact that, although the IGM component is also expected to contribute to the covariance matrix in Eq. (3.3), its contribution would be subdominant in broad redshift range as shown in Fig. 1.

In a similar fashion, we can define the Fisher matrix from CMB power spectrum measurements:

$$F_{ab}^{(\text{CMB})} = \sum_l \frac{2l+1}{2} \text{Tr} \left[\mathbf{C}_l^{(\text{CMB})^{-1}} \frac{\partial \mathbf{C}_l^{(\text{CMB})}}{\partial p_a} \mathbf{C}_l^{(\text{CMB})^{-1}} \frac{\partial \mathbf{C}_l^{(\text{CMB})}}{\partial p_b} \right], \quad (3.4)$$

where $[\mathbf{C}_l]_{PQ}^{(\text{CMB})} \equiv C_{l,PQ}^{(\text{CMB})} + N_{l,PQ}^{(\text{CMB})}$ is the covariance matrix of measured CMB anisotropies, with the subscript $P(Q)$ indicating the temperature or E-mode polarization. Following Ref. [32], we approximate the CMB noise power spectrum $N_{l,PQ}^{(\text{CMB})}$ as

$$N_{l,PQ} = \delta_{PQ} \theta_{\text{FWHM}}^2 \sigma_P^2 \exp \left[l(l+1) \frac{\theta_{\text{FWHM}}^2}{8 \ln 2} \right], \quad (3.5)$$

where θ_{FWHM} are the full width at half maximum of the Gaussian beam, and σ_P is the root-mean-square of the instrumental noise per pixel.

4 Constraints on spectral runnings of primordial power spectrum

In order to demonstrate the potential of the angular power spectrum of 21 cm line fluctuations from minihalos, here we present expected constraints on the power spectrum of primordial curvature perturbation, particularly focusing on the spectral index n_s and its runnings α_s, β_s .

4.1 Runnings of the spectral index

Conventionally the scale-dependence of the primordial power spectrum is given by the power law form with the spectral index n_s , which is often assumed to be constant in scale (wavenumber). However, the spectral index can generally depend on the scale and such scale-dependence could give us detailed information on the primordial power spectrum $\mathcal{P}_s(k) := k^3 P_\zeta(k)/2\pi^2$, where $P_\zeta(k)$ is defined as

$$\langle \zeta(\mathbf{k})\zeta(\mathbf{k}') \rangle = (2\pi)^3 \delta^{(3)}(\mathbf{k} + \mathbf{k}') P_\zeta(k), \quad (4.1)$$

with ζ being the primordial curvature perturbations. Here, $\delta^{(3)}(\mathbf{k} + \mathbf{k}')$ is a 3-dimensional Dirac's delta function and $P_\zeta(k)$ determines the initial condition of the linear matter power spectrum denoted by $P(k)$ through the Poisson equation. By taking into account the scale-dependence of the spectral index, we can perturbatively write \mathcal{P}_s as

$$\mathcal{P}_s(k) = A_s \left(\frac{k}{k_0} \right)^{n_s - 1 + \frac{1}{2}\alpha_s \ln(k/k_0) + \frac{1}{3!}\beta_s \ln^2(k/k_0)}, \quad (4.2)$$

where A_s , k_0 and n_s are respectively the amplitude, the pivot scale and the spectral index, and we have expanded \mathcal{P}_s in terms of $\ln k$ up to the 2nd order. The expansion coefficients in the 1st and 2nd orders are denoted as $\alpha_s (\equiv dn_s/d\ln k)$ and $\beta_s (\equiv d^2n_s/d\ln^2 k)$, which we call the running and the quadratic running of n_s , respectively. In the framework of the slow-roll inflation, the runnings such as α_s and β_s can be explicitly written down by using the so-called slow-roll parameters. We provide those expressions in Appendix A. In principle, we can expand \mathcal{P}_s up to arbitrarily higher orders and hence we also, in Appendix A, give expressions for higher order runnings in terms of the slow-roll parameters not only for the single-field case but also for the multi-field case.

4.2 Forecasts based on the Fisher matrix analysis

Let us investigate the expected constraints on primordial power spectrum in future 21cm line observations, especially focusing on the parameters n_s , α_s and β_s . The determination of these parameters requires precise measurements of cosmological perturbations over a wide range of scales, which can be achieved by combining observations of the CMB and 21 cm line fluctuations. For 21 cm line observations, we in this paper adopt the specifications of SKA [23] and FFFT [24]. In addition to 21 cm line fluctuations from minihalos, we also combine CMB observations with the expected sensitivities of Planck [35] and CORE [36]^{#1}. The survey parameters we adopt are summarized in Tables 1 and 2. In our analysis, we assume a flat Λ CDM model and the pivot scale k_0 is fixed to 0.05 Mpc^{-1} as in the Planck analysis. In addition to n_s, α_s and β_s , we also include the following parameters in the Fisher matrix: the reduced Hubble parameter h , baryon and CDM densities ω_b and ω_c , the reionization

^{#1} While the survey parameters we adopt here are somewhat different from those in the most recent proposal of the CORE mission, our results do not differ significantly.

	SKA	FFTT
total effective area A_{tot} [m ²]	10 ⁵	10 ⁷
bandwidth $\Delta\nu$ [MHz]		1
beam width $\Delta\theta$ [arcmin]		9
integration time t [hour]		1000

Table 1. Specification of 21 cm surveys.

	Planck			CORE				
band frequency [GHz]	100	147	217	105	135	165	195	225
beam width $\Delta\theta$ [arcmin]	9.9	7.2	4.9	10.0	7.8	6.4	5.4	4.7
Temperature noise Δ_T [μK arcmin]	31.3	20.1	28.5	2.68	2.63	2.67	2.63	2.64
Polarization noise Δ_P [μK arcmin]	44.2	33.3	49.4	4.63	4.55	4.61	4.54	4.57

Table 2. Specification of CMB surveys.

optical depth τ_{reion} , and the amplitude of the primordial power spectrum A_s . The fiducial parameters are assumed to be the same as the ones used in Fig. 2.

Fig. 3 shows derivatives of $C_l^{(21\text{cm})}$ with respect to parameters n_s (red), α_s (green), β_s (blue), which captures the dependence of $C_l^{(21\text{cm})}(z, z')$ on these parameters. For reference, the fiducial $C_l^{(21\text{cm})}$ is also depicted (purple). When $C_l^{(21\text{cm})}$ is highly dependent on a parameter, the derivative of $C_l^{(21\text{cm})}$ becomes large in the figure. Here, fixing the central redshift $(z + z')/2 = 5$, we take $z - z' = 0$ (top-left), 0.2 (top-right), 0.4 (bottom-left), 0.6 (bottom-right). From the figure, we can see the following tendencies: For $\Delta z = 0$ (top-left), n_s affects $C_l^{(21\text{cm})}$ in a scale-dependent way, however α_s and β_s only changes the overall amplitude of $C_l^{(21\text{cm})}$. For $\Delta z = 0.2$ (top-right), n_s and α_s can both affect $C_l^{(21\text{cm})}$ scale-dependently, but β_s only gives the change in the overall amplitude. For $\Delta z = 0.4$ (bottom-left) and 0.6 (bottom-right), all parameters only affect the amplitude of $C_l^{(21\text{cm})}$ up to $l \sim \mathcal{O}(100)$. These trends can be understood as follows. The spectral index n_s (and the running α_s in some cases) can affect the matter fluctuations $P(k)$ directly on (observable) large scales, which can affect $C_l^{(21\text{cm})}$ in a scale-dependent manner. On the other hand, the quadratic running parameter β_s affects $C_l^{(21\text{cm})}$ largely only through the overall amplitude since this parameter changes $C_l^{(21\text{cm})}$ mainly through the minihalo abundances dn/dM , which reflects $P(k)$ at scales too small to be directly measured in the angular power spectrum [20]. If there were no effects on the shape of $C_l^{(21\text{cm})}$, the parameters would be indistinguishable. However, in reality, the response of the overall amplitude to the higher order running parameters is dependent on redshifts, which enables to disentangle such parameters. Such redshift dependence can be seen by comparing panels of Fig. 3, each of which has distinct $\Delta z = z - z'$.

Fig. 4 shows constraints on the primordial power spectrum from 21 cm, CMB, and combinations of these observations. In Table 3 we summarize expected 1σ constraints on n_s , α_s and β_s from different combinations of observations. In the figure, we have assumed 21 cm line observations can measure the signal from minihalos at a redshift between $z_{\text{min}} = 6$ and $z_{\text{max}} = 20$.

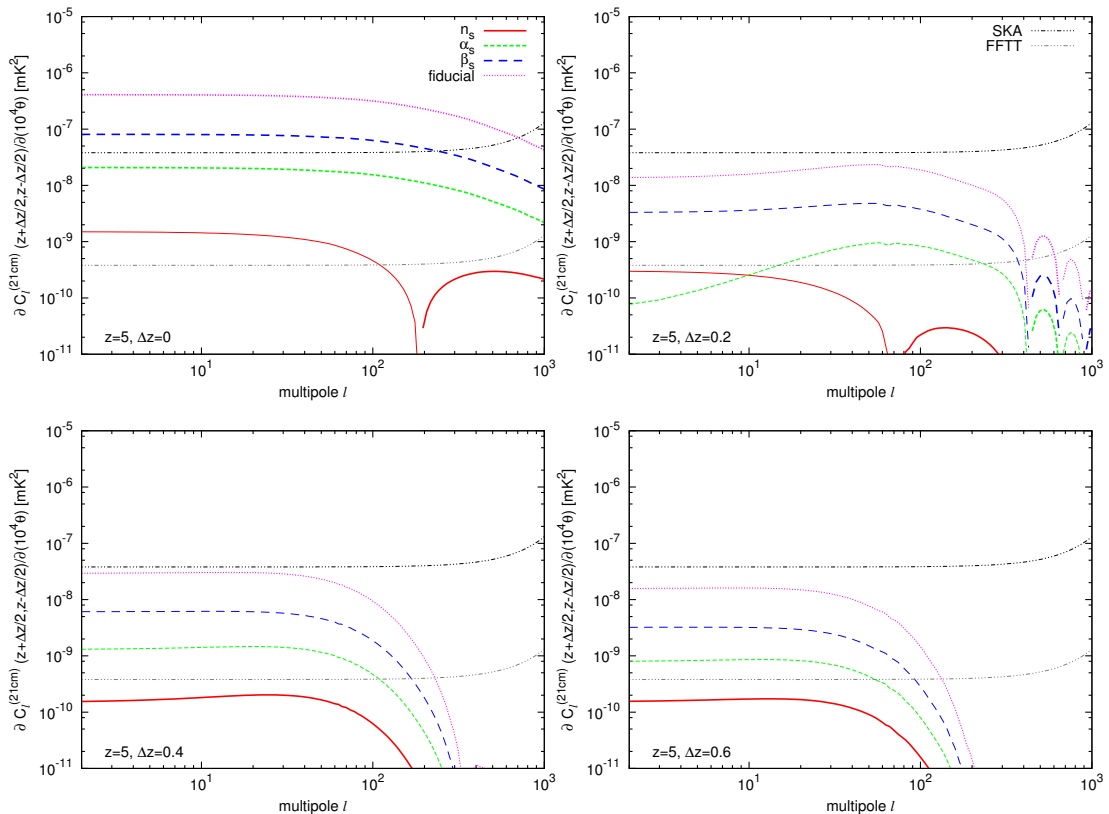


Figure 3. Dependence of $C_l^{(21\text{cm})}$ on the parameters of the primordial power spectrum. Plotted are the derivative of $C_l^{(21\text{cm})}$ with respect to $\theta = n_s$ (red), α_s (green) and β_s (blue), divided by 10^4 for visualization purpose. We also show the fiducial $C_l^{(21\text{cm})}$ (divided by 10^2) for comparison (purple). The noise power spectra for SKA and FFTT are also plotted (black). The central redshift is fixed to $z = 5$ and the redshift difference is varied as 0 (top-left), 0.2 (top-right), 0.4 (bottom-left), 0.6 (bottom-right).

First of all, it is remarkable in the figure that 21 cm line power spectrum from minihalos (i.e. SKA and FFTT) is competitive or even more powerful in comparison with the CMB observations (i.e. Planck and COre) as a probe of the primordial power spectrum. In particular, $C_l^{(21\text{cm})}$ can measure β_s more tightly than $C_l^{(\text{CMB})}$. This is because the abundance of minihalos is sensitive to the linear matter fluctuations at very small scales, which is difficult to be measured directly. Meanwhile, $C_l^{(21\text{cm})}$ can also measure fluctuations at larger scales through the spectral shape, which constrains n_s and α_s .

Once observations of 21 cm line fluctuations from minihalos and the CMB are combined, we can probe matter fluctuations over a wide range of scales. Combinations of these two different observations offer a great advantage by the lever-arm effect when we try to constrain the primordial power spectrum that is close to the power-law as in Eq. (4.2). In other words, combinations of these observations can break parameter degeneracies that each observation suffers from by itself. This is most notable in Fig. 4 when Planck and SKA are combined.

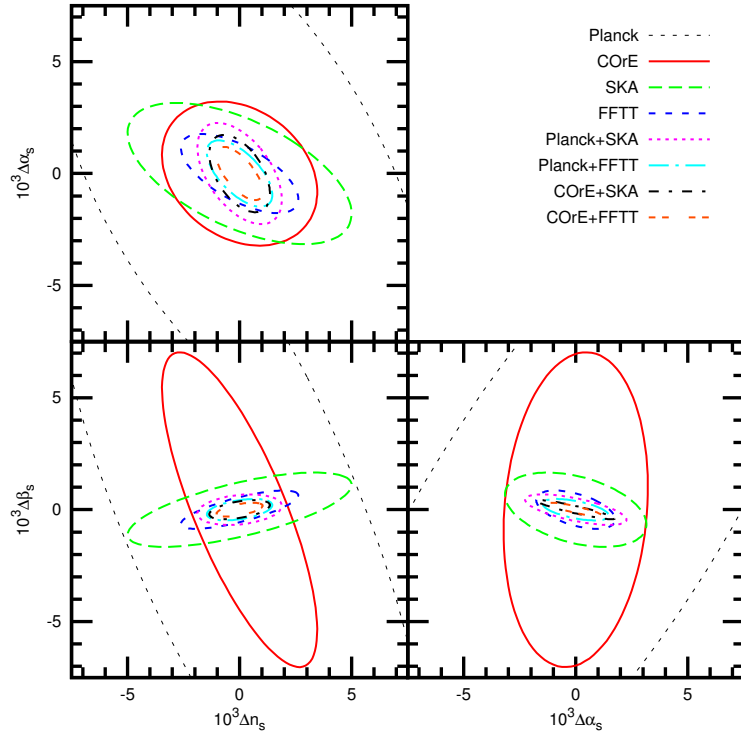


Figure 4. Expected constraints on the primordial power spectrum from observations of 21 cm signals from minihalos in combination with the CMB. Contours depict 1σ errors with other cosmological parameters being marginalized. We assume 21 cm signals from minihalos can be measured down to $z_{\min} = 6$.

	$10^{-3}\Delta n_s$	$10^{-3}\Delta\alpha_s$	$10^{-3}\Delta\beta_s$
Planck	7.7	10.7	15.1
COrE	3.2	2.9	6.5
SKA	4.6	2.9	1.5
FFTT	2.4	1.6	0.79
Planck+SKA	1.7	2.0	0.63
Planck+FFTT	1.3	1.3	0.44
COrE+SKA	1.2	1.6	0.39
COrE+FFTT	0.95	1.1	0.28

Table 3. Constraints on parameters for the primordial power spectrum. For 21 cm observations, $z_{\min} = 6$ is assumed.

On the other hand, as can be read off by Eq. (3.2), the signal-to-noise ratio in observations of the 21cm signal from minihalos rapidly increases at low redshifts. Therefore, the

	z_{\min}	$10^{-3}\Delta n_s$	$10^{-3}\Delta\alpha_s$	$10^{-3}\Delta\beta_s$
Planck+SKA	4	1.4	1.4	0.40
	6	1.7	2.0	0.63
	8	2.3	3.0	0.85
	10	3.6	4.7	1.2
COre+FFTT	4	0.85	0.96	0.24
	6	0.95	1.1	0.28
	8	1.0	1.2	0.31
	10	1.1	1.3	0.33

Table 4. Dependence of the constraints on z_{\min} for the data sets, Planck+SKA and COre+FFTT.

resultant constraints are expected to be dependent of z_{\min} , the minimum redshift until when minihalos can be observed. In order to examine the dependence, we have evaluated expected (marginalized) 1σ uncertainties for the determination of n_s , α_s and β_s from two datasets, Planck+SKA and COre+FFTT with z_{\min} being 4, 6 (baseline), 8 and 10, which are summarized in Table 4. As expected, the constraints become less tight as z_{\min} is increased although the changes are not so significant. For example, the change of z_{\min} from 6 to 8 degrades the constraint on each of the parameters by around 50% for Planck+SKA. On the other hand, for the combination of COre+FFTT, the degradation becomes modest; between $z_{\min} = 6$ and 10, the constraint changes only by 10%.

4.3 Implication for the constraint on the inflationary models

Now let us consider the implication of our results for the constraint on the inflationary models. As shown in the Planck paper [5], the parameter plane in terms of the spectral index and the tensor-to-scalar ratio (n_s - r plane) is useful to constrain the inflationary models (for the predictions of various inflation models, see [37]). In fact, it implies that the simple chaotic inflationary models with the inflaton’s potential $V \propto \phi^n$ are almost ruled out for $n \gtrsim 2$ and the so-called R^2 -inflation model [38–40] seems to be favored. However, once the multi-field inflationary models are taken into account such as the curvaton model [41–43], modulated reheating model [44, 45] and so on, where a light scalar field other than inflaton exists and its fluctuations also contribute to primordial fluctuations, not only R^2 -inflation but also several inflationary models are well inside the allowed region on the n_s - r plane [46–57]. It is well-known that one of the powerful tools to distinguish single-field inflationary models from the multi-field ones is the non-Gaussianity of the primordial fluctuations, especially the so-called local-type non-Gaussianity. In general, the single-field models predict small local-type non-Gaussianity, while multi-field models could generate relatively larger one. However, at the level of current constraint on non-Gaussianity from Planck [58], we cannot differentiate between single-field and multi-field models.

Here, we discuss the potential of the runnings of the spectral index to distinguish among inflation models, having our Fisher analysis results given in the previous section in mind. In the following, we choose some representatives of single-field and multi-field models and apply the expressions for the spectral parameters provided in Appendix A. As examples for single-field models, we consider the R^2 -inflation and brane-inflation. For multi-field models, the natural- and inverse monomial-spectator models are investigated. We take the model

parameters in such a way that these models are consistent with the current observations and hardly distinguished from one another to date (see Section 4.3.5).

4.3.1 R^2 -inflation

R^2 -inflation was proposed in Refs. [38–40], where the inflationary phase can be realized by the higher order curvature term, R^2 . It has been known that this model corresponds to the single-field inflation in Einstein frame with the potential of

$$V(\phi) = \Lambda^4 \left(1 - e^{-\sqrt{2/3}\phi/M_{\text{pl}}}\right)^2. \quad (4.3)$$

Based on the slow-roll approximation, the e -folding number measured from the time when the pivot scale k_0 left the Hubble radius during the inflation to the end of inflation can be estimated as

$$N_0 = \int_{t_0}^{t_e} H dt \simeq -\frac{1}{M_{\text{pl}}^2} \int_{\phi_0}^{\phi_e} \frac{V}{V'} d\phi, \quad (4.4)$$

where the index e and 0 respectively represent the time when the inflation ends and the pivot scale k_0 left the Hubble radius during the inflation. For the R^2 -inflation model, this e -folding number can be obtained as

$$N_0 \simeq \frac{3}{4} e^{\sqrt{2/3}\phi_0/M_{\text{pl}}}, \quad (4.5)$$

where we keep only the leading term. The slow-roll parameters are also given in terms of N_0 as

$$\epsilon \simeq \frac{3}{4} \frac{1}{N_0^2}, \quad \eta \simeq -\frac{1}{N_0}, \quad \xi^{(2)} \simeq \frac{1}{N_0^3}, \quad \sigma^{(3)} \simeq -\frac{1}{N_0^3}, \quad \dots, \quad (4.6)$$

where we have assumed $N_0 \gg 1$. For the single-field models, since the tensor-to-scalar ratio and the spectral index are respectively given by

$$n_s - 1 = -6\epsilon + 2\eta, \quad r = 16\epsilon, \quad (4.7)$$

we can estimate n_s and r from the e -folding number N_0 for the R^2 -inflation as

$$n_s - 1 \simeq -\frac{2}{N_0} (\simeq -(3.3 - 4) \times 10^{-2}), \quad r = \frac{12}{N_0^2} (\simeq (3.3 - 4.8) \times 10^{-3}) \quad (\text{for } N_0 = 50 - 60), \quad (4.8)$$

at the leading order in N_0 .

The scales of the primordial fluctuations on which we focus here are around $20 \text{ Mpc}^{-1} < k < 500 \text{ Mpc}^{-1}$ as we have discussed. In Fig. 5, we plot the power spectrum of the primordial curvature perturbations generated from R^2 -inflation, numerically calculated one and approximated by the power-law expansion form. From this figure, one can find that at minihalos' scales the power spectrum only including n_s deviates from the numerically-evaluated power spectrum. On the other hand, by using the expression for the power spectrum up to α_s seems to be in good agreement with the numerical result. Hence we need to take account of a higher order running to test inflationary models using observations of small scales such as

minihalos. Based on Appendix A, α_s and β_s in the R^2 -inflation can be respectively obtained as

$$\alpha_s \simeq -\frac{2}{N_0^2} (\simeq -(5.5 - 8) \times 10^{-4}), \quad \beta_s \simeq -\frac{4}{N_0^3} (\simeq -(1.9 - 3.2) \times 10^{-5}) \quad (\text{for } N_0 = 50 - 60), \quad (4.9)$$

at the leading order in N_0 .

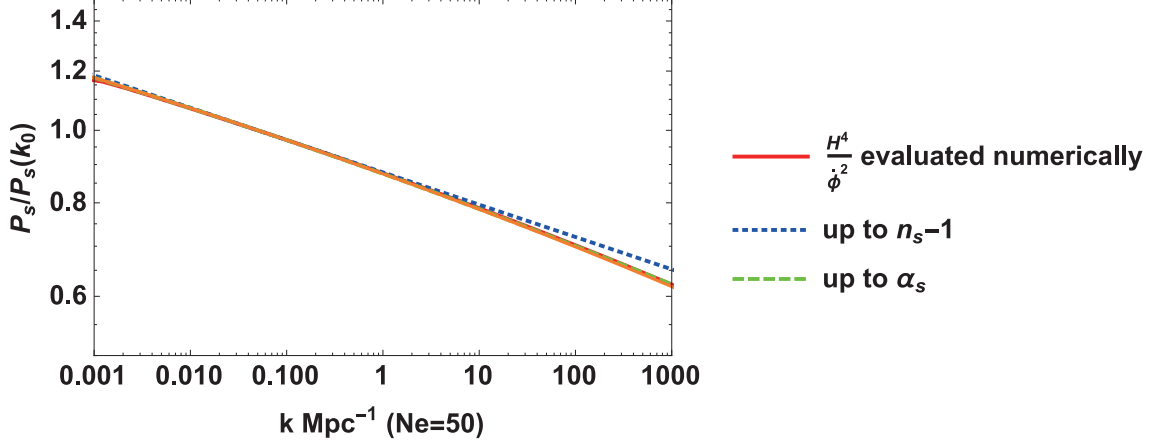


Figure 5. The power spectrum of the primordial curvature perturbations generated from the R^2 -inflation. The red line is obtained by numerically calculating the background dynamics and evaluating $H^4/\dot{\phi}^2$. The blue dotted line corresponds to the one calculated from the power-law form given by (A.1) including up to n_s , and the green dashed line corresponds to that up to α_s .

4.3.2 Brane inflation

The potential of the brane inflation models is phenomenologically given as (see [37, 59] and references therein)

$$V(\phi) = V_0 \left[1 - \left(\frac{\phi}{\mu} \right)^{-p} \right], \quad (4.10)$$

where V_0 represents the energy scale of the model and p and μ are also model parameters.

The slow-roll parameters in this model are given as

$$\begin{aligned} \epsilon &= \frac{p^2}{2\tilde{\mu}^2\tilde{\phi}_0^2(\tilde{\phi}_0^p - 1)^2}, & \eta &= -\frac{p(p+1)}{\tilde{\mu}^2\tilde{\phi}_0^2(\tilde{\phi}_0^p - 1)}, \\ \xi^{(2)} &= \frac{p^2(p+1)(p+2)}{\tilde{\mu}^4\tilde{\phi}_0^4(\tilde{\phi}_0^p - 1)^2}, & \sigma^{(3)} &= -\frac{p^3(p+1)(p+2)(p+3)}{\tilde{\mu}^6\tilde{\phi}_0^6(\tilde{\phi}_0^p - 1)^3}, \end{aligned} \quad (4.11)$$

where we have defined $\tilde{\mu}$ and $\tilde{\phi}_0$ as $\tilde{\mu} \equiv \mu/M_{\text{pl}}$ and $\tilde{\phi}_0 \equiv \phi_0/\mu$. The number of e -folds can be expressed as

$$N_0 = \frac{\tilde{\mu}^2}{2p} \left[\frac{2}{p+2} \left(\tilde{\phi}_0^{p+2} - \tilde{\phi}_e^{p+2} \right) - \left(\tilde{\phi}_0^2 - \tilde{\phi}_e^2 \right) \right], \quad (4.12)$$

with ϕ_e being the value of ϕ at the end of inflation, at which one of the slow-roll parameters exceeds unity. Assuming that $\tilde{\phi}_0 \gg 1$ and $\tilde{\phi}_0 \gg \tilde{\phi}_e$ in Eq. (4.12), $\tilde{\phi}_0$ can be approximated by

$$\tilde{\phi}_0 \simeq \left[p(p+2) \frac{N_e}{\tilde{\mu}^2} \right]^{1/(p+2)}. \quad (4.13)$$

The spectral index n_s , the tensor-to-scalar ratio r , the running parameters α_s and β_s can be calculated in the same way by putting the slow-roll parameters given in Eq. (4.11) into the formulas Eqs. (A.5) and (A.6).

4.3.3 Natural-spectator model

Next we consider a multi-field model. To predict the spectral index, its higher order runnings and the tensor-to-scalar ratio, we do not have to specify the spectator field model itself, but need to specify the potential for the spectator field χ . Here we take a quadratic potential for χ as $V(\chi) = \frac{1}{2}m_\chi^2\chi^2$ with m_χ being the mass of the spectator field and assume that m_χ is much smaller than the Hubble parameter during inflation, which gives $\eta_\chi \simeq 0$ and $\xi_\chi^{(2)} = \sigma_\chi^{(3)} = 0$. Furthermore, we also have to specify the inflaton potential.

A simplest natural inflation model is characterized by the potential [60, 61]:

$$V(\phi) = \Lambda^4 \left[1 - \cos\left(\frac{\phi}{f}\right) \right] \quad (0 \leq \phi \leq \pi f), \quad (4.14)$$

where Λ denotes the energy scale of the model and f corresponds to some breaking scale which determines the curvature of the potential. Based on the slow-roll approximation, the e -folding number for the natural inflation is expressed as

$$N_0 = \frac{f^2}{M_{\text{pl}}^2} \ln \left| \frac{\cos^2(\phi_e/2f)}{\cos^2(\phi_0/2f)} \right|, \quad (4.15)$$

where ϕ_e denotes the field value at the end of inflation. The slow-roll parameters are respectively given by

$$\begin{aligned} \epsilon &= \frac{M_{\text{pl}}^2 \cos^2(\phi_0/2f)}{2f^2 \sin^2(\phi_0/2f)}, & \eta &= \frac{M_{\text{pl}}^2 (1 - 2 \sin^2(\phi_0/2f))}{f^2 (2 \sin^2(\phi_0/2f))}, \\ \xi^{(2)} &= -\frac{M_{\text{pl}}^4 \cos^2(\phi_0/2f)}{f^4 \sin^2(\phi_0/2f)}, & \sigma^{(3)} &= -\frac{M_{\text{pl}}^6 \cos^2(\phi_0/2f) (1 - 2 \sin^2(\phi_0/2f))}{f^6 (2 \sin^2(\phi_0/2f))}. \end{aligned} \quad (4.16)$$

The end of inflation is defined by $\epsilon = 1$, and it gives

$$\cos^2 \frac{\phi_e}{2f} = \frac{2f^2/M_{\text{pl}}^2}{1 + 2f^2/M_{\text{pl}}^2}. \quad (4.17)$$

The prediction for the spectral index, its higher order runnings and the tensor-to-scalar ratio can be calculated by putting the slow-roll parameters Eqs. (4.16) into the formulas (A.20), (A.21), (A.22) and (A.26) given in Appendix A.

4.3.4 Inverse monomial-spectator model

The potential of the inverse monomial inflation model is given by

$$V(\phi) = V_0 \left(\frac{\phi}{M_{\text{pl}}} \right)^{-p}, \quad (4.18)$$

where V_0 represents the energy scale of the model and p is assumed to be positive. In the slow-roll approximation, the number of e -folds is written as

$$N_0 = \frac{1}{2p} \left[\left(\frac{\phi_e}{M_{\text{pl}}} \right)^2 - \left(\frac{\phi_0}{M_{\text{pl}}} \right)^2 \right]. \quad (4.19)$$

Notice that the inflation does not end by the slow-roll violation in this model, hence it needs some mechanism to exit from the inflationary era. Here we just assume some mechanism works to stop the inflation. The slow-roll parameters are given by

$$\begin{aligned} \epsilon &= \frac{1}{2} p^2 \left(\frac{\phi_0}{M_{\text{pl}}} \right)^{-2}, & \eta &= p(p+1) \left(\frac{\phi_0}{M_{\text{pl}}} \right)^{-2}, \\ \xi^{(2)} &= p^2(p+1)(p+2) \left(\frac{\phi_0}{M_{\text{pl}}} \right)^{-4}, & \sigma^{(3)} &= p^3(p+1)(p+2)(p+3) \left(\frac{\phi_0}{M_{\text{pl}}} \right)^{-6}. \end{aligned} \quad (4.20)$$

From Eq. (4.19), one can express ϕ_0 as

$$\left(\frac{\phi_0}{M_{\text{pl}}} \right)^2 = \left(\frac{\phi_e}{M_{\text{pl}}} \right)^2 - 2pN_0. \quad (4.21)$$

As mentioned above, the inflation should end by some mechanism (not by the slow-roll violation), ϕ_e depends on the mechanism. Since varying ϕ_e corresponds to changing ϕ_0 as seen from Eq. (4.21), we take ϕ_0 as a phenomenological parameter which is chosen to obtain n_s and r in accordance with observational constraint.

4.3.5 Predictions of the models

In Fig. 6, we plot the predictions for r , n_s , α_s and β_s for the R^2 -inflation (yellow), brane-inflation (magenta), natural-spectator (green) and inverse monomial-spectator (purple) models. The upper left, upper right and lower panels show the predictions in the $n_s - r$, $n_s - \alpha_s$ and $\alpha_s - \beta_s$ planes, respectively.

For the R^2 model, we take $50 < N_0 < 60$, which gives a very good fit to the current Planck observations [5]. For other models, we choose the values of the parameters such that the prediction for n_s and r become almost the same with those for R^2 inflation, which can be seen in the upper left panel of Fig. 6. Also some of the parameters are chosen to give a correct amplitude for the primordial power spectrum. For the brane inflation, we consider the case with $p = 4$ and $\mu = 2.6M_{\text{pl}}$, and assume $43 < N_0 < 52$. For the natural-spectator model, we take $f = 3.5M_{\text{pl}}$ and $51 < N_0 < 54$ for the inflaton sector and assume the fractional contribution of the spectator, Q_χ (defined in Eq. (A.18)), to be $0.5 < Q_\chi < 0.6$. For the inverse monomial-spectator model, we consider the case with $p = 6$ and take $Q_\chi \simeq 0.98$ (or precisely speaking, by using R defined in Eq. (A.19), we take $75 < R < 80$.) The field value at the end of inflation ϕ_e is varied to be tuned to give almost the degenerate prediction for n_s and r with R^2 inflation as depicted in the upper left panel of Fig. 6.

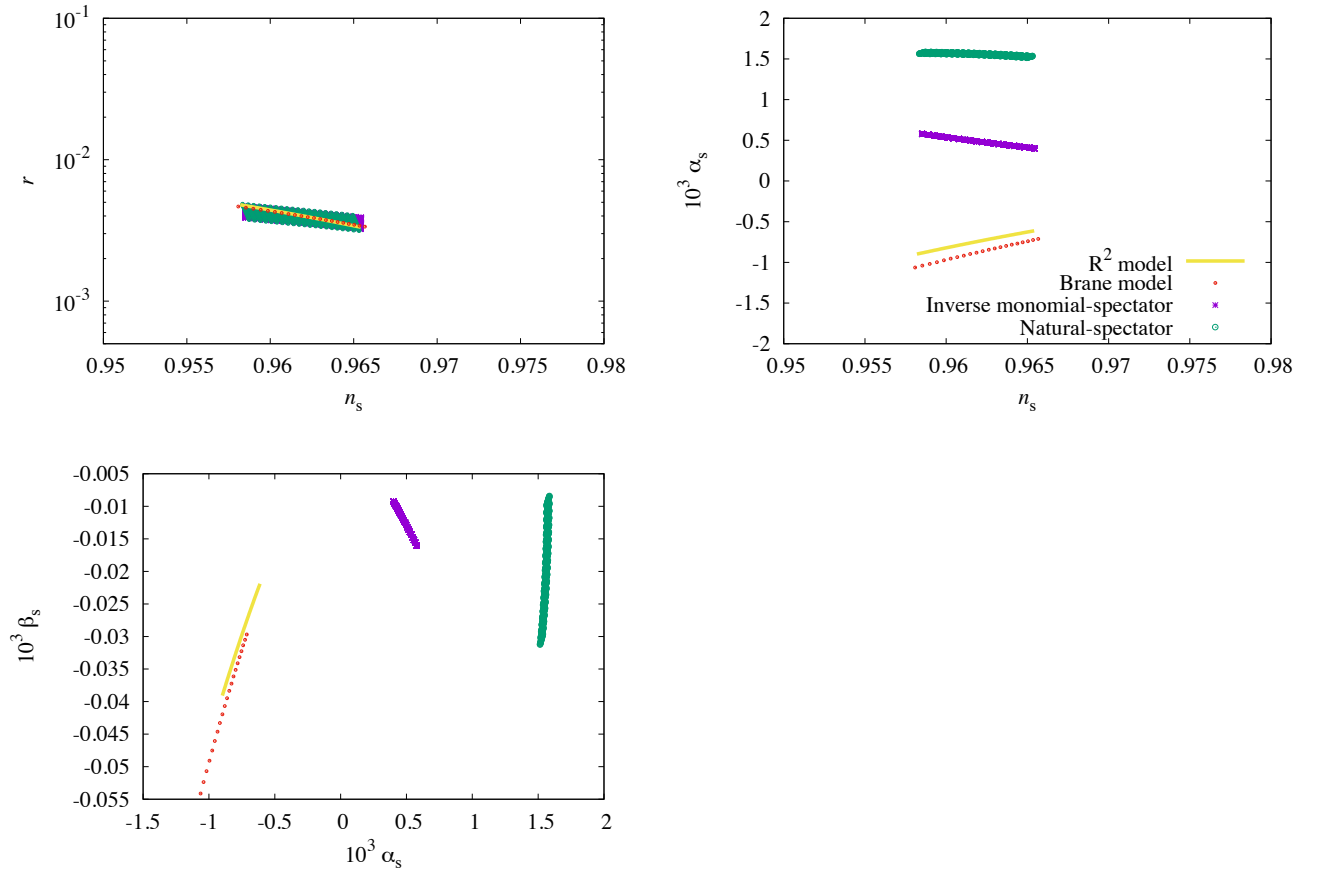


Figure 6. Predictions for n_s , α_s , β_s and r for the R^2 -inflation (yellow), brane inflation (orange), the natural-spectator model (green) and the inverse monomial-spectator model (purple). The upper left panel shows the predictions in the $n_s - r$ plane, and the upper right one shows those in the $n_s - \alpha_s$ plane. The lower panel shows the predictions in the $\alpha_s - \beta_s$ plane.

As seen in the upper left in Fig. 6, models discussed here can give almost degenerate predictions for n_s and r , however, when we compare the predictions of these models in the $n_s - \alpha_s$ and the $\alpha_s - \beta_s$ planes, we can see that those models give different runnings, which would be helpful to distinguish the model. It should be noted here that some models could be easily differentiated by using the expected constraint from future mininalo observations on the $n_s - \alpha_s$ and $\alpha_s - \beta_s$ planes shown in Fig. 4. On the other hand, some models are still difficult to be distinguished from the expected constraint investigated in this paper.

5 Conclusion

In this paper, we have developed the formalism to use the angular power spectrum of 21 cm line fluctuations from minihalos to constrain cosmological models, instead of adopting the analysis based on the pixel variance, which have been used in previous studies. Our formulation can take account of cross-correlations not only in angular domains, but also in redshift ones. The advantage in considering such cross-correlations over the simple pixel variance is that we can decode the scale-dependences on top of the increase in the statistics.

By making use of the formalism, we have forecasted constraints on the power spectrum of primordial perturbations from future observations of 21 cm line fluctuations from minihalos in combination with the CMB. In particular, we have focused on the spectral index n_s and its runnings α_s and β_s . Our results exhibit the potential of the angular power spectrum of 21 cm line fluctuations as a promising probe of primordial power spectrum. Particularly, the synergy in combination with the CMB is remarkable due to the lever-arm effect since 21 cm fluctuations from minihalos are sensitive to those on small scales, while CMB observations probe those on large scales. For any combinations of CMB and 21 cm observations (Planck+SKA, Planck+FFTT, CORe+SKA, CORe+FFTT), the spectral runnings can be probed down to the level of $\alpha_s \sim \mathcal{O}(10^{-3})$ and $\beta_s \sim \mathcal{O}(10^{-4})$ (see Table 3).

We have also discussed implications of future constraints on the runnings for differentiating inflationary models. For the purpose, we considered several representative models of single- and multi-field models including R^2 -inflation. We have shown that future sensitivities of 21 cm signals from minihalos on the runnings α_s and β_s would be helpful to differentiate inflationary models in some cases. Although we have just looked at some representative models, a more exhaustive study of inflationary models from the viewpoint of the spectral runnings would give more insight to really understand the mechanism of inflation.

Acknowledgments

TT thanks Sami Nurmi for helpful discussions. This work is partially supported by JSPS KAKENHI Grant Number 15K05084 (TT), 15K17646 (HT), 15K17659 (SY), MEXT KAKENHI Grant Number 15H05888 (TT, SY), 16H01103 (SY), and IBS under the project code, IBS-R018-D1 (TS).

Appendix

A Expressions for higher order runnings with slow-roll parameters

In Eq. (4.2), we have expanded the primordial power spectrum \mathcal{P}_s up to the 2nd order. However, in principle, the primordial power spectrum can be expanded up to arbitrarily higher orders. Here we truncate the expansion at the 4th order, in which \mathcal{P}_s is given by

$$\mathcal{P}_s(k) = A_s \left(\frac{k}{k_0} \right)^{n_s - 1 + \frac{1}{2}\alpha_s \ln(k/k_0) + \frac{1}{3!}\beta_s \ln^2(k/k_0) + \frac{1}{4!}\gamma_s \ln^3(k/k_0) + \frac{1}{5!}\delta_s \ln^4(k/k_0)}, \quad (\text{A.1})$$

where the runnings $\alpha_s, \beta_s, \gamma_s$ and δ_s are defined as

$$\begin{aligned}\alpha_s &\equiv \left. \frac{d^2 \ln \mathcal{P}_s(k)}{(d \ln k)^2} \right|_{k=k_0}, & \beta_s &\equiv \left. \frac{d^3 \ln \mathcal{P}_s(k)}{(d \ln k)^3} \right|_{k=k_0}, \\ \gamma_s &\equiv \left. \frac{d^4 \ln \mathcal{P}_s(k)}{(d \ln k)^4} \right|_{k=k_0}, & \delta_s &\equiv \left. \frac{d^5 \ln \mathcal{P}_s(k)}{(d \ln k)^5} \right|_{k=k_0}.\end{aligned}\tag{A.2}$$

Below we give explicit expressions for these runnings using the slow-roll parameters for the single-field and multi-field models.

A.1 Single-field case

Assuming a slow-roll single-field inflation model with a canonical kinetic term, n_s and the running parameters can be explicitly written down with the slow-roll parameters, which are defined using the inflaton potential $V(\phi)$ as

$$\begin{aligned}\epsilon &\equiv \frac{1}{2} M_{\text{pl}}^2 \left(\frac{V'}{V} \right)^2, & \eta &\equiv M_{\text{pl}}^2 \frac{V''}{V}, & \xi^{(2)} &\equiv M_{\text{pl}}^4 \frac{V'V'''}{V^2}, \\ \sigma^{(3)} &\equiv M_{\text{pl}}^6 \frac{(V')^2 V^{(4)}}{V^3}, & \tau^{(4)} &\equiv M_{\text{pl}}^8 \frac{(V')^3 V^{(5)}}{V^4}, & \zeta^{(5)} &\equiv M_{\text{pl}}^{10} \frac{(V')^4 V^{(6)}}{V^5},\end{aligned}\tag{A.3}$$

where a prime denotes the derivative with respect to ϕ . Using these slow-roll parameters, the spectral index and the runnings are given by:

$$n_s - 1 = -6\epsilon + 2\eta,\tag{A.4}$$

$$\alpha_s = -24\epsilon^2 + 16\epsilon\eta - 2\xi^{(2)},\tag{A.5}$$

$$\beta_s = -192\epsilon^3 + 192\epsilon^2\eta - 32\epsilon\eta^2 - 24\epsilon\xi^{(2)} + 2\eta\xi^{(2)} + 2\sigma^{(3)},\tag{A.6}$$

$$\begin{aligned}\gamma_s &= -2304\epsilon^4 + 3072\epsilon^3\eta - 1024\epsilon^2\eta^2 - 384\epsilon^2\xi^{(2)} + 64\epsilon\eta^3 + 148\epsilon\eta\xi^{(2)} + 36\epsilon\sigma^{(3)} \\ &\quad - 6\eta\sigma^{(3)} - 2\eta^2\xi^{(2)} - 2(\xi^{(2)})^2 - 2\tau^{(4)},\end{aligned}\tag{A.7}$$

$$\begin{aligned}\delta_s &= -36864\epsilon^5 + 61440\epsilon^4\eta - 30720\epsilon^3\eta^2 - 7680\epsilon^3\xi^{(2)} + 4736\epsilon^2\eta^3 + 5448\epsilon^2\eta\xi^{(2)} \\ &\quad + 744\epsilon^2\sigma^{(3)} - 128\epsilon\eta^4 - 652\epsilon\eta^2\xi^{(2)} - 164\epsilon(\xi^{(2)})^2 - 340\epsilon\eta\sigma^{(3)} - 52\epsilon\tau^{(4)} \\ &\quad + 2\eta^3\xi^{(2)} + 14\eta^2\sigma^{(3)} + 8\eta(\xi^{(2)})^2 + 12\eta\tau^{(4)} + 10\xi^{(2)}\sigma^{(3)} + 2\zeta^{(5)}.\end{aligned}\tag{A.8}$$

The tensor-to-scalar ratio is given by

$$r = 16\epsilon.\tag{A.9}$$

A.2 Multi-field case

When a light scalar field χ other than the inflaton ϕ exists during the inflationary epoch^{#2}, such a scalar field can also acquire primordial fluctuations and affect the present-day density fluctuations as in the curvaton model [41–43], the modulated reheating model [44, 45] and so on. In general, fluctuations from the inflaton can also contribute to the primordial fluctuations, and therefore the power spectrum can be given by the sum of those contributions^{#3}:

$$\mathcal{P}_s(k) = \mathcal{P}_s^{(\phi)}(k) + \mathcal{P}_s^{(\chi)}(k),\tag{A.10}$$

^{#2} Such another (light) scalar field is sometimes called a spectator field since it does not affect the inflationary dynamics.

^{#3} This kind of model is called mixed inflaton and spectator field models, which has been studied in the context of the curvaton and modulated reheating models [46–57].

where $\mathcal{P}_s^{(\phi)}(k)$ and $\mathcal{P}_s^{(\chi)}(k)$ are the primordial power spectra generated by the inflaton ϕ and another spectator field χ . Due to the fact that the energy density of χ is subdominant during inflation, the spectral index and its runnings for $\mathcal{P}_s^{(\chi)}$ are different from those for $\mathcal{P}_s^{(\phi)}$ which are given in Eqs. (A.4)–(A.8). To write down the spectral index and its runnings for $\mathcal{P}_s^{(\chi)}$, we also need to define the slow-roll parameters for χ :

$$\begin{aligned}\eta_\chi &\equiv \frac{U''}{3H_*^2}, & \xi_\chi^{(2)} &\equiv \frac{U'U'''}{(3H_*^2)^2}, & \sigma_\chi^{(3)} &\equiv \frac{(U')^2U^{(4)}}{(3H_*^2)^3}, \\ \tau_\chi^{(4)} &\equiv \frac{(U')^3U^{(5)}}{(3H_*^2)^4}, & \zeta_\chi^{(5)} &\equiv \frac{(U')^4U^{(6)}}{(3H_*^2)^5},\end{aligned}\quad (\text{A.11})$$

where U is a potential for χ field and a prime indicates the derivative with respect to the χ field. A superscript (i) denotes the i -th derivative. H_* is the Hubble parameter at the horizon exit during inflation. By using these slow-roll parameters along with those defined for ϕ provided in Eqs. (A.3), the spectral index and its runnings for χ are given as^{#4}

$$n_s^{(\chi)} - 1 = -2\epsilon + 2\eta_\chi, \quad (\text{A.12})$$

$$\alpha_s^{(\chi)} = -8\epsilon^2 + 4\epsilon\eta + 4\epsilon\eta_\chi - 2\xi_\chi^{(2)}, \quad (\text{A.13})$$

$$\beta_s^{(\chi)} = -64\epsilon^3 + 56\epsilon^2\eta + 24\epsilon^2\eta_\chi - 8\epsilon\eta^2 - 8\epsilon\eta\eta_\chi - 4\epsilon\xi_\chi^{(2)} - 12\epsilon\xi_\chi^{(2)} + 2\eta_\chi\xi_\chi^{(2)} + 2\sigma_\chi^{(3)}, \quad (\text{A.14})$$

$$\begin{aligned}\gamma_s^{(\chi)} &= -768\epsilon^4 + 944\epsilon^3\eta + 240\epsilon^3\eta_\chi - 288\epsilon^2\eta^2 - 160\epsilon^2\eta\eta_\chi - 88\epsilon^2\xi_\chi^{(2)} - 120\epsilon^2\xi_\chi^{(2)} \\ &\quad + 16\epsilon\eta^3 + 16\epsilon\eta^2\eta_\chi + 28\epsilon\eta\xi_\chi^{(2)} + 8\epsilon\eta_\chi\xi_\chi^{(2)} + 32\epsilon\eta\xi_\chi^{(2)} + 24\epsilon\eta_\chi\xi_\chi^{(2)} + 4\epsilon\sigma_\chi^{(3)} \\ &\quad + 24\epsilon\sigma_\chi^{(3)} - 2\eta_\chi^2\xi_\chi^{(2)} - 6\eta_\chi\sigma_\chi^{(3)} - 2(\xi_\chi^{(2)})^2 - 2\tau_\chi^{(4)},\end{aligned}\quad (\text{A.15})$$

$$\begin{aligned}\delta_s^{(\chi)} &= -12288\epsilon^5 + 19360\epsilon^4\eta + 3360\epsilon^4\eta_\chi - 9120\epsilon^3\eta^2 - 3360\epsilon^3\eta\eta_\chi - 2000\epsilon^3\xi_\chi^{(2)} - 1680\epsilon^3\xi_\chi^{(2)} \\ &\quad + 1312\epsilon^2\eta^3 + 800\epsilon^2\eta^2\eta_\chi + 1296\epsilon^2\eta\xi_\chi^{(2)} + 240\epsilon^2\eta_\chi\xi_\chi^{(2)} + 960\epsilon^2\eta\xi_\chi^{(2)} + 360\epsilon^2\eta_\chi\xi_\chi^{(2)} \\ &\quad + 128\epsilon^2\sigma_\chi^{(3)} + 360\epsilon^2\sigma_\chi^{(3)} - 32\epsilon\eta^4 - 32\epsilon\eta^3\eta_\chi - 132\epsilon\eta^2\xi_\chi^{(2)} - 56\epsilon\eta\eta_\chi\xi_\chi^{(2)} - 28\epsilon(\xi_\chi^{(2)})^2 \\ &\quad - 80\epsilon\eta^2\xi_\chi^{(2)} - 80\epsilon\eta\eta_\chi\xi_\chi^{(2)} - 40\epsilon\eta_\chi^2\xi_\chi^{(2)} - 40\epsilon\xi_\chi^{(2)}\xi_\chi^{(2)} - 40\epsilon(\xi_\chi^{(2)})^2 - 44\epsilon\eta\sigma_\chi^{(3)} - 8\epsilon\eta_\chi\sigma_\chi^{(3)} \\ &\quad - 80\epsilon\eta\sigma_\chi^{(3)} - 120\epsilon\eta_\chi\sigma_\chi^{(3)} - 4\epsilon\tau_\chi^{(4)} - 40\epsilon\tau_\chi^{(4)} + 2\eta_\chi^3\xi_\chi^{(2)} + 14\eta_\chi^2\sigma_\chi^{(3)} + 8\eta_\chi(\xi_\chi^{(2)})^2 \\ &\quad + 12\eta_\chi\tau_\chi^{(4)} + 10\xi_\chi^{(2)}\sigma_\chi^{(3)} + 2\zeta_\chi^{(5)}.\end{aligned}\quad (\text{A.16})$$

Since $\mathcal{P}_s^{(\phi)}$ and $\mathcal{P}_s^{(\chi)}$ have different scale dependences, they should be treated separately. However, we can define the effective spectral index and its runnings by using the total power spectrum as

$$n_s^{(\text{eff})} - 1 = \frac{d \ln(\mathcal{P}_s^{(\phi)}(k) + \mathcal{P}_s^{(\chi)}(k))}{d \ln k}, \quad (\text{A.17})$$

with which we can describe the power spectrum as if there is only one power spectrum.

To explicitly express the effective spectral index and its runnings with the slow-roll parameters, we also need to define the fraction of the contribution to the (total) power spectrum from ϕ and χ fields as

$$Q_\phi \equiv \frac{\mathcal{P}_s^{(\phi)}(k_0)}{\mathcal{P}_s^{(\phi)}(k_0) + \mathcal{P}_s^{(\chi)}(k_0)}, \quad Q_\chi \equiv \frac{\mathcal{P}_s^{(\chi)}(k_0)}{\mathcal{P}_s^{(\phi)}(k_0) + \mathcal{P}_s^{(\chi)}(k_0)}, \quad (\text{A.18})$$

^{#4} Here we assume that there is no coupling between the inflaton and the spectator fields.

where these quantities are to be evaluated at the pivot scale. In some literature, the ratio R between $\mathcal{P}_s^{(\chi)}$ and $\mathcal{P}_s^{(\phi)}$ is also used to characterize the contribution from the spectator

$$R \equiv \frac{\mathcal{P}_s^{(\chi)}(k_0)}{\mathcal{P}_s^{(\phi)}(k_0)} \left(= \frac{Q_\chi}{1 - Q_\chi} \right), \quad (\text{A.19})$$

which is again defined at the pivot scale. With these variables, the spectral index and its runnings are given by

$$n_s^{(\text{eff})} - 1 = Q_\phi(n_s^{(\phi)} - 1) + Q_\chi(n_s^{(\chi)} - 1), \quad (\text{A.20})$$

$$\alpha_s^{(\text{eff})} = Q_\phi\alpha_s^{(\phi)} + Q_\chi\alpha_s^{(\chi)} + Q_\phi Q_\chi(\Delta n_s)^2, \quad (\text{A.21})$$

$$\beta_s^{(\text{eff})} = Q_\phi\beta_s^{(\phi)} + Q_\chi\beta_s^{(\chi)} + 3Q_\phi Q_\chi\Delta n_s\Delta\alpha_s - Q_\phi Q_\chi(Q_\phi - Q_\chi)(\Delta n_s)^3, \quad (\text{A.22})$$

$$\begin{aligned} \gamma_s^{(\text{eff})} = & Q_\phi\gamma_s^{(\phi)} + Q_\chi\gamma_s^{(\chi)} + Q_\phi Q_\chi(4\Delta n_s\Delta\beta_s + 3(\Delta\alpha_s)^2) \\ & - 6Q_\phi Q_\chi(Q_\phi - Q_\chi)(\Delta n_s)^2\Delta\alpha_s + \{Q_\phi Q_\chi(Q_\phi - Q_\chi)^2 - 2Q_\phi^2 Q_\chi^2\}(\Delta n_s)^4, \end{aligned} \quad (\text{A.23})$$

$$\begin{aligned} \delta_s^{(\text{eff})} = & Q_\phi\delta_s^{(\phi)} + Q_\chi\delta_s^{(\chi)} + Q_\phi Q_\chi(10\Delta\alpha_s\Delta\beta_s + 5\Delta n_s\Delta\gamma_s) \\ & - Q_\phi Q_\chi(Q_\phi - Q_\chi)\{10(\Delta n_s)^2\Delta\beta_s + 15\Delta n_s(\Delta\alpha_s)^2\} \\ & + \{10Q_\phi Q_\chi(Q_\chi - Q_\phi)^2 - 20Q_\phi^2 Q_\chi^2\}(\Delta n_s)^3\Delta\alpha_s \\ & - \{Q_\phi Q_\chi(Q_\chi - Q_\phi)^3 - 8Q_\phi^2 Q_\chi^2(Q_\chi - Q_\phi)\}(\Delta n_s)^5, \end{aligned} \quad (\text{A.24})$$

where

$$\Delta n_s = n_s^{(\phi)} - n_s^{(\chi)}, \quad \Delta\alpha_s = \alpha_s^{(\phi)} - \alpha_s^{(\chi)}, \quad \Delta\beta_s = \beta_s^{(\phi)} - \beta_s^{(\chi)}, \quad \Delta\gamma_s = \gamma_s^{(\phi)} - \gamma_s^{(\chi)}, \quad \Delta\delta_s = \delta_s^{(\phi)} - \delta_s^{(\chi)}. \quad (\text{A.25})$$

In the limits where $Q_\phi \rightarrow 0$ and $Q_\chi \rightarrow 0$, the expressions become the same as the pure spectator and inflaton cases, respectively.

The tensor-to-scalar ratio in multi-field models is given by

$$r^{(\text{multi})} = 16\epsilon Q_\chi, \quad (\text{A.26})$$

from which one can see that the tensor-to-scalar ratio is generally suppressed in multi-field models.

B Constraints on higher order spectral runnings

In the main text, we have truncated the expansion at the quadratic order running β_s . However, minihalos can probe small scale fluctuations at $20 \text{ Mpc}^{-1} < k < 500 \text{ Mpc}^{-1}$. Therefore, we can also probe the higher order runnings such as the cubic and quartic runnings, γ_s and δ_s . In Fig. 7, the expected constraints on n_s and the runnings for the case with $z_{\text{min}} = 6$ are given and their 1σ sensitivities are summarized in Table 5. Also, as discussed in the text, the constraints depend on the minimum redshift. In Table 6, the dependence of 1σ errors is also summarized for the combinations of Planck+SKA and CoRE+FFTT.

References

- [1] R. Adam *et al.* [Planck Collaboration], *Astron. Astrophys.* **594**, A1 (2016)
doi:10.1051/0004-6361/201527101 [arXiv:1502.01582 [astro-ph.CO]].

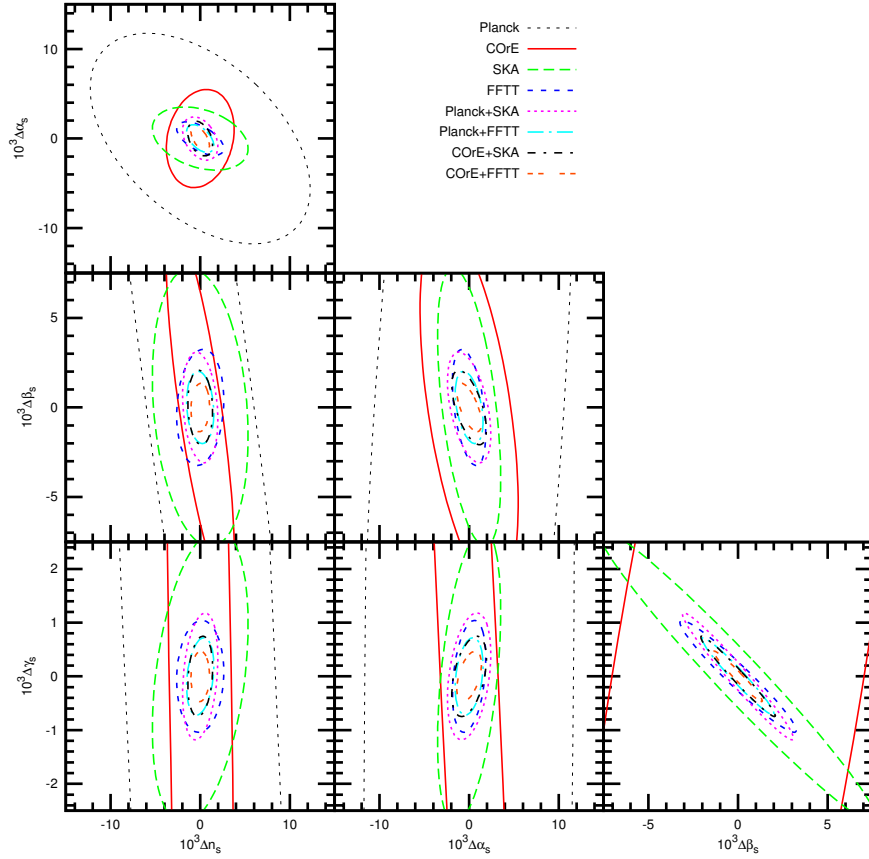


Figure 7. Constraints on the spectral index n_s and its runnings up to the cubic order. For 21 cm line observations, $z_{\min} = 6$ is assumed.

	$10^3 \Delta n_s$	$10^3 \Delta \alpha_s$	$10^3 \Delta \beta_s$	$10^3 \Delta \gamma_s$
Planck	11.3	10.8	37.4	32.1
COre	3.5	5.0	9.4	14.2
SKA	4.9	3.3	7.2	2.5
FFTT	2.4	1.7	3.0	0.96
Planck+SKA	1.8	2.2	2.8	1.0
Planck+FFTT	1.4	1.4	1.8	0.66
COre+SKA	1.2	1.7	1.9	0.69
COre+FFTT	0.95	1.2	1.2	0.43

Table 5. Expected 1σ sensitivities for the spectral index n_s and its runnings up to the cubic order. For 21 cm line observations, $z_{\min} = 6$ is assumed.

[2] P. A. R. Ade *et al.* [Planck Collaboration], *Astron. Astrophys.* **594**, A13 (2016)
doi:10.1051/0004-6361/201525830 [arXiv:1502.01589 [astro-ph.CO]].

	z_{\min}	$10^3\Delta n_s$	$10^3\Delta\alpha_s$	$10^3\Delta\beta_s$	$10^3\Delta\gamma_s$
Planck+SKA	4	1.5	1.6	2.3	0.78
	6	1.8	2.2	2.9	1.1
	8	2.4	3.2	3.2	1.3
	10	3.7	4.7	4.5	1.9
COre+FFTT	4	0.86	1.1	1.1	0.38
	6	0.95	1.3	1.3	0.43
	8	1.1	1.4	1.3	0.45
	10	1.2	1.6	1.4	0.48

Table 6. Dependence of the constraints on z_{\min} for Planck+SKA and COre+FFTT.

- [3] S. Alam *et al.* [BOSS Collaboration], [arXiv:1607.03155 [astro-ph.CO]].
- [4] M. Betoule *et al.* [SDSS Collaboration], *Astron. Astrophys.* **568**, A22 (2014) doi:10.1051/0004-6361/201423413 [arXiv:1401.4064 [astro-ph.CO]].
- [5] P. A. R. Ade *et al.* [Planck Collaboration], *Astron. Astrophys.* **594** (2016) A20 doi:10.1051/0004-6361/201525898 [arXiv:1502.02114 [astro-ph.CO]].
- [6] Q. G. Huang, S. Wang and W. Zhao, *JCAP* **1510**, no. 10, 035 (2015) doi:10.1088/1475-7516/2015/10/035 [arXiv:1509.02676 [astro-ph.CO]].
- [7] J. Errard, S. M. Feeney, H. V. Peiris and A. H. Jaffe, *JCAP* **1603**, no. 03, 052 (2016) doi:10.1088/1475-7516/2016/03/052 [arXiv:1509.06770 [astro-ph.CO]].
- [8] D. Alonso, J. Dunkley, B. Thorne and S. Naess, *Phys. Rev. D* **95**, no. 4, 043504 (2017) doi:10.1103/PhysRevD.95.043504 [arXiv:1608.00551 [astro-ph.CO]].
- [9] K. N. Abazajian *et al.* [CMB-S4 Collaboration], arXiv:1610.02743 [astro-ph.CO].
- [10] D. Barron *et al.*, arXiv:1702.07467 [astro-ph.IM].
- [11] K. Kohri, Y. Oyama, T. Sekiguchi and T. Takahashi, *JCAP* **1310**, 065 (2013) doi:10.1088/1475-7516/2013/10/065 [arXiv:1303.1688 [astro-ph.CO]].
- [12] J. B. Muñoz, E. D. Kovetz, A. Raccanelli, M. Kamionkowski and J. Silk, arXiv:1611.05883 [astro-ph.CO].
- [13] J. B. Dent, D. A. Easson and H. Tashiro, *Phys. Rev. D* **86**, 023514 (2012) doi:10.1103/PhysRevD.86.023514 [arXiv:1202.6066 [astro-ph.CO]].
- [14] G. Cabass, A. Melchiorri and E. Pajer, *Phys. Rev. D* **93**, no. 8, 083515 (2016) doi:10.1103/PhysRevD.93.083515 [arXiv:1602.05578 [astro-ph.CO]].
- [15] I. T. Iliev, P. R. Shapiro, A. Ferrara and H. Martel, *Astrophys. J.* **572**, 123 (2002) doi:10.1086/341869 [astro-ph/0202410].
- [16] I. T. Iliev, E. Scannapieco, H. Martel and P. R. Shapiro, *Mon. Not. Roy. Astron. Soc.* **341**, 81 (2003) doi:10.1046/j.1365-8711.2003.06410.x [astro-ph/0209216].
- [17] H. Shimabukuro, K. Ichiki, S. Inoue and S. Yokoyama, *Phys. Rev. D* **90**, no. 8, 083003 (2014) doi:10.1103/PhysRevD.90.083003 [arXiv:1403.1605 [astro-ph.CO]].
- [18] T. Sekiguchi and H. Tashiro, *JCAP* **1408**, 007 (2014) doi:10.1088/1475-7516/2014/08/007 [arXiv:1401.5563 [astro-ph.CO]].
- [19] Y. Takeuchi and S. Chongchitnan, *Mon. Not. Roy. Astron. Soc.* **439**, no. 1, 1125 (2014) doi:10.1093/mnras/stu059 [arXiv:1311.2585 [astro-ph.CO]].

- [20] T. Sekiguchi, H. Tashiro, J. Silk and N. Sugiyama, JCAP **1403**, 001 (2014) doi:10.1088/1475-7516/2014/03/001 [arXiv:1311.3294 [astro-ph.CO]].
- [21] S. Chongchitnan and J. Silk, Mon. Not. Roy. Astron. Soc. **426**, L21 (2012) doi:10.1111/j.1745-3933.2012.01315.x [arXiv:1205.6799 [astro-ph.CO]].
- [22] H. Tashiro, T. Sekiguchi and J. Silk, JCAP **1401** (2014) 013 doi:10.1088/1475-7516/2014/01/013 [arXiv:1310.4176 [astro-ph.CO]].
- [23] <https://www.skatelescope.org>
- [24] M. Tegmark and M. Zaldarriaga, Phys. Rev. D **79**, 083530 (2009) doi:10.1103/PhysRevD.79.083530 [arXiv:0805.4414 [astro-ph]].
- [25] P. R. Shapiro and I. T. Iliev, Mon. Not. Roy. Astron. Soc. **307**, 203 (1999) doi:10.1046/j.1365-8711.1999.02609.x [astro-ph/9810164].
- [26] H. J. Mo and S. D. M. White, Mon. Not. Roy. Astron. Soc. **282**, 347 (1996) doi:10.1093/mnras/282.2.347 [astro-ph/9512127].
- [27] P. Madau, A. Meiksin and M. J. Rees, Astrophys. J. **475**, 429 (1997) doi:10.1086/303549 [astro-ph/9608010].
- [28] P. R. Shapiro, I. T. Iliev and A. C. Raga, Mon. Not. Roy. Astron. Soc. **348**, 753 (2004) doi:10.1111/j.1365-2966.2004.07364.x [astro-ph/0307266].
- [29] R. Adam *et al.* [Planck Collaboration], doi:10.1051/0004-6361/201628897 arXiv:1605.03507 [astro-ph.CO].
- [30] R. Barkana and A. Loeb, Phys. Rept. **349**, 125 (2001) doi:10.1016/S0370-1573(01)00019-9 [astro-ph/0010468].
- [31] N. Kaiser, Mon. Not. Roy. Astron. Soc. **227**, 1 (1987).
- [32] L. Knox, Phys. Rev. D **52**, 4307 (1995) [arXiv:astro-ph/9504054].
- [33] S. Furlanetto, S. P. Oh and F. Briggs, Phys. Rept. **433**, 181 (2006) [astro-ph/0608032].
- [34] M. Tegmark, A. Taylor and A. Heavens, Astrophys. J. **480**, 22 (1997) doi:10.1086/303939 [astro-ph/9603021].
- [35] J. Tauber *et al.* [Planck Collaboration], astro-ph/0604069.
- [36] <http://www.core-mission.org>
- [37] J. Martin, C. Ringeval and V. Vennin, Phys. Dark Univ. **5-6**, 75 (2014) doi:10.1016/j.dark.2014.01.003 [arXiv:1303.3787 [astro-ph.CO]].
- [38] A. A. Starobinsky, Phys. Lett. **91B**, 99 (1980). doi:10.1016/0370-2693(80)90670-X
- [39] H. Nariai and K. Tomita, Prog. Theor. Phys. **46**, 776 (1971). doi:10.1143/PTP.46.776
- [40] K. Tomita, arXiv:1603.07621 [gr-qc].
- [41] K. Enqvist and M. S. Sloth, Nucl. Phys. B **626**, 395 (2002) [arXiv:hep-ph/0109214].
- [42] D. H. Lyth and D. Wands, Phys. Lett. B **524**, 5 (2002) [arXiv:hep-ph/0110002].
- [43] T. Moroi and T. Takahashi, Phys. Lett. B **522**, 215 (2001) [Erratum-ibid. B **539**, 303 (2002)] [arXiv:hep-ph/0110096].
- [44] G. Dvali, A. Gruzinov, M. Zaldarriaga, Phys. Rev. **D69**, 023505 (2004). [astro-ph/0303591].
- [45] L. Kofman, [astro-ph/0303614].
- [46] D. Langlois and F. Vernizzi, Phys. Rev. D **70**, 063522 (2004) [arXiv:astro-ph/0403258];
- [47] G. Lazarides, R. R. de Austri and R. Trotta, Phys. Rev. D **70**, 123527 (2004) [hep-ph/0409335].

- [48] T. Moroi, T. Takahashi and Y. Toyoda, Phys. Rev. D **72**, 023502 (2005) [arXiv:hep-ph/0501007];
- [49] T. Moroi and T. Takahashi, Phys. Rev. D **72**, 023505 (2005) [arXiv:astro-ph/0505339];
- [50] K. Ichikawa, T. Suyama, T. Takahashi and M. Yamaguchi, Phys. Rev. D **78**, 023513 (2008) [arXiv:0802.4138 [astro-ph]].
- [51] K. Ichikawa, T. Suyama, T. Takahashi and M. Yamaguchi, Phys. Rev. D **78**, 063545 (2008) [arXiv:0807.3988 [astro-ph]].
- [52] T. Suyama, T. Takahashi, M. Yamaguchi and S. Yokoyama, JCAP **1012**, 030 (2010) [arXiv:1009.1979 [astro-ph.CO]].
- [53] J. Fonseca and D. Wands, JCAP **1206**, 028 (2012) [arXiv:1204.3443 [astro-ph.CO]].
- [54] K. Enqvist and T. Takahashi, JCAP **1310** (2013) 034 [arXiv:1306.5958 [astro-ph.CO]].
- [55] V. Vennin, K. Koyama and D. Wands, JCAP **1511**, 008 (2015) [arXiv:1507.07575 [astro-ph.CO]].
- [56] T. Fujita, M. Kawasaki and S. Yokoyama, JCAP **1409**, 015 (2014) doi:10.1088/1475-7516/2014/09/015 [arXiv:1404.0951 [astro-ph.CO]].
- [57] K. Enqvist, T. Sekiguchi and T. Takahashi, JCAP **1604**, no. 04, 057 (2016) [arXiv:1511.09304 [astro-ph.CO]].
- [58] P. A. R. Ade *et al.* [Planck Collaboration], Astron. Astrophys. **594**, A17 (2016) doi:10.1051/0004-6361/201525836 [arXiv:1502.01592 [astro-ph.CO]].
- [59] L. Lorenz, J. Martin and C. Ringeval, JCAP **0804**, 001 (2008) doi:10.1088/1475-7516/2008/04/001 [arXiv:0709.3758 [hep-th]].
- [60] K. Freese, J. A. Frieman and A. V. Olinto, Phys. Rev. Lett. **65**, 3233 (1990). doi:10.1103/PhysRevLett.65.3233
- [61] F. C. Adams, J. R. Bond, K. Freese, J. A. Frieman and A. V. Olinto, Phys. Rev. D **47**, 426 (1993) doi:10.1103/PhysRevD.47.426 [hep-ph/9207245].